

Atomistic simulations of surface segregation of defects in solid oxide electrolytes

Hark B. Lee*, Friedrich B. Prinz, Wei Cai

Department of Mechanical Engineering, Stanford University, CA 94305-4040, USA

Received 23 September 2009; received in revised form 30 November 2009; accepted 3 December 2009

Available online 22 January 2010

Abstract

We performed atomistic simulations of yttria-stabilized zirconia (YSZ) and gadolinia-doped ceria (GDC) to study the segregation of point defects near (100) surfaces. A hybrid Monte Carlo–molecular dynamics algorithm was developed to sample the equilibrium distributions of dopant cations and oxygen vacancies. The simulations predict an increase of dopant concentration near the surface, which is consistent with experimental observations. Oxygen vacancies are also found to segregate in the first anion layer beneath the surface and to be depleted in the subsequent anion layers. While the ionic size mismatch between dopant and host cations has been considered as a driving force for dopant segregation to the surface, our simulations show that the correlation between individual point defects plays a dominant role in determining their equilibrium distributions. This correlation effect leads to more pronounced dopant segregation in GDC than in YSZ, even though the size mismatch between dopant and host cations is much greater in YSZ than in GDC.

© 2009 Acta Materialia Inc. Published by Elsevier Ltd. All rights reserved.

Keywords: Segregation; Monte Carlo; Molecular dynamics; Yttria-stabilized zirconia; Gadolinia-doped ceria

1. Introduction

Yttria-stabilized zirconia (YSZ) and gadolinia-doped ceria (GDC) are widely used electrolyte materials for solid oxide fuel cells (SOFCs) due to their high ionic conductivities. In a number of experimental studies, dopant cations (i.e. Y^{3+} in YSZ and Gd^{3+} in GDC) have been observed to segregate to the surfaces [1–11] and grain boundaries. Dopant segregation at the surface is important in fuel cell applications because it can affect the near-surface chemical reactions and ionic transport of the electrolytes. A clear understanding of surface segregation will also shed light on the mechanism of grain boundary segregation, about which many fundamental questions still remain unanswered. Surface segregation of dopant cations becomes especially important in thin film structures that are fabricated by pulsed laser deposition (PLD) [12], chemical

vapor deposition (CVD) [13] or atomic layer deposition (ALD) [14] techniques and have a high density of grain boundaries as well as a large surface-to-volume ratio.

Dopant segregation in solid oxides has been studied both experimentally and theoretically. Existing experimental techniques are mostly limited in their spatial resolutions (on the order of a few nanometers), which makes it very challenging to uncover the detailed distributions of point defects on the atomic scale. Moreover, it is currently not possible to directly measure the spatial distribution of oxygen vacancies, which are the main charge carriers in the fuel cell operation.

Defect distributions near the surfaces and grain boundaries of YSZ have also been studied by space-charge theory [15–20], which predicts dopant segregation and oxygen vacancy depletion in the vicinity of the interfaces. Since it is a continuum theory, the applicability of the space-charge theory becomes questionable when the density profile it predicts varies rapidly over the length scale of a few lattice spacings. Furthermore, the mean-field approximation made in these studies does not account for the correlation

* Corresponding author. Tel.: +1 650 575 7150.

E-mail addresses: hblee@stanford.edu (H.B. Lee), fprinz@stanford.edu (F.B. Prinz), caiwei@stanford.edu (W. Cai).

between individual point defects, even though the most general form of space-charge theory can incorporate it [21–24].

In this study, we carry out atomistic simulations of defect segregation in YSZ and GDC, in which the correlation between individual defects can be taken into account explicitly. Molecular dynamics (MD) simulations based on empirical interatomic pair-potentials have provided valuable insights into the diffusion of oxygen ions and defect ordering in YSZ and GDC [25–42]. Unfortunately, cations hardly diffuse in the time scale of typical MD simulations, and therefore direct MD simulations are unable to capture interfacial segregation of dopant cations. To resolve this issue, we developed a hybrid Monte Carlo–molecular dynamics (MC–MD) algorithm that can overcome the limited time scale of conventional MD simulations and simulate defect segregation. This is the first atomistic model able to predict the equilibrium distributions of dopant cations and oxygen vacancies near the surfaces of YSZ and GDC. Our simulation results show a substantial increase of dopant concentration near the surfaces, which is consistent with experimental observations. The simulation also predicts different equilibrium dopant distributions in YSZ and GDC, which can be explained from the differences in the correlation between dopant cations and oxygen vacancies [25,29,35,36,38,40,41,43–50]. While this dopant–vacancy interaction was not considered in the application of space-charge theory to YSZ [15–20], we find it to be the dominant factor in determining the equilibrium distributions of defects near the surface.

This paper is organized as follows. In Section 2, we describe the atomistic models, initialization of the simulation cells and the hybrid MC–MD algorithm. The simulation results are presented in Section 3. In Section 4, we discuss the driving forces of defect segregation based on these results. A brief summary is given in Section 5.

2. Methods

YSZ and GDC crystals are assumed to be fully ionic and the interactions between ions are modeled by the combination of the short-range Born–Mayer–Buckingham (BMB)

potential and the long-range Coulomb potential [39,51,52]. The functional form of the interatomic potentials and the parameters for both materials are given in the Appendix. An implicit assumption is made that these interatomic potentials are valid for the surface, although they are empirically fitted to the properties of the bulk crystals.

2.1. Initializing structures

YSZ and GDC have CaF_2 (cubic) crystal structures and each unit cell contains four cations (Zr^{4+} or Y^{3+} in YSZ, Ce^{4+} or Gd^{3+} in GDC) that form a face-centered cubic (fcc) cation sublattice. The eight tetrahedral interstitial sites of each fcc unit cell are occupied by oxygen ions or vacancies, which form a simple cubic (SC) anion sublattice. The initial structures for the atomistic simulations are prepared in the following four steps.

First, cubic ZrO_2 and CeO_2 perfect crystals approximately $6 \text{ nm} \times 3 \text{ nm} \times 3 \text{ nm}$ in size are created with x , y and z axes corresponding to the [100], [010] and [001] crystal orientations, respectively. The simulation cells are then extended by 50% in the x -direction. This creates 100 surfaces on both sides of the crystal. Periodic boundary conditions are applied in all three directions, resulting in a periodic array of free-standing thin films with a 3 nm separation between neighboring films.

Second, dopant cations are introduced by altering the species of randomly chosen host cations (e.g. from Zr^{4+} to Y^{3+} in YSZ) and oxygen vacancies are created by removing arbitrarily selected oxygen ions. To maintain the charge balance of the system, one oxygen vacancy is created for every two dopant cations. The doping concentration of yttria or gadolinia is set to 10 mol.% for both materials. The structure of YSZ thin film after this step is shown in Fig. 1a, where the left surface is terminated by cations and the right surface by anions. The asymmetric distribution of electric charge results in an energetically unfavorable structure, which will disappear shortly after in the subsequent equilibration steps.

Third, the structures are relaxed by the conjugate gradient (CG) relaxation to a local energy minimum.

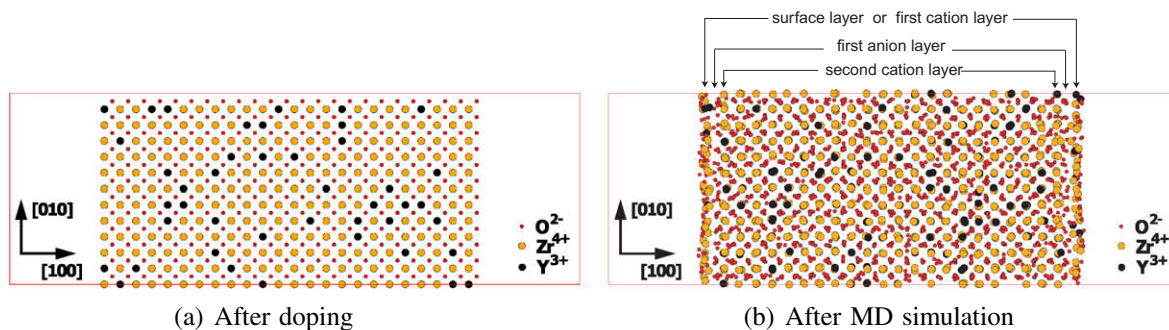


Fig. 1. Simulation snapshots of a 10 mol.% YSZ thin film. (a) Before relaxation and (b) after CG relaxation and 100 ps of MD (NPT) simulation at $T = 2000 \text{ K}$ and $p = 0 \text{ MPa}$.

Finally, the simulation cells are equilibrated by MD simulations in an NPT ensemble using the velocity Verlet integrator with a time step of 0.5 fs. The Nose–Hoover thermostat [53–55] and the Parrinello–Rahman method [56] are employed to control the temperature at 2000 K and the stress at zero. The structure of the YSZ thin film after this step is shown in Fig. 1b, where it maintains clear crystallinity even in the close vicinity of the surfaces. During the MD simulations, we observe substantial diffusion of oxygen ions and, as a consequence, both left and right sides of the crystals are covered by half monolayers of oxygen ions, which we define as surface layers. The oxygen-terminated (001) surface of YSZ qualitatively agrees with medium-energy ion scattering (MEIS) experiments and ab initio calculations [57–59]. However, no cation moves away from its randomly chosen initial site during the equilibration even at high temperatures. The lack of cation diffusion can be attributed to its high activation energy barrier, the absence of cation vacancies and the limited time scale of the MD simulations. This implies that a different algorithm is required to sample the equilibrium distribution of dopant cations.

2.2. Hybrid MC–MD algorithm

To further equilibrate the atomistic structures, we develop a MC algorithm that alters the cation distributions. The MC trial move is designed to switch the positions of a randomly chosen pair of dopant (Y^{3+} in YSZ and Gd^{3+} in GDC) and host (Zr^{4+} in YSZ and Ce^{4+} in GDC) cations and help sample the equilibrium distribution of the dopants. MD still remains as a part of the algorithm to allow collective moves of all ions. It enables the equilibration of the overall structure as well as the redistribution of the oxygen vacancies. The MD part is periodically executed during the simulation and this combination of MC and MD results in a hybrid MC–MD algorithm. In the following, we explain the MC switch moves in detail, using YSZ as an example.

Every MC step starts with a trial switch move, in which a pair of randomly chosen Y^{3+} and Zr^{4+} ions are swapped. The trial move is accepted with a probability P_{acc} that depends on the potential energy change it introduces, according to the Metropolis algorithm [60],

$$P_{acc} = \min \left[1, \exp \left(-\frac{\Delta E}{k_B T} \right) \right] \quad (1)$$

where ΔE is the potential energy difference before and after an MC trial move, k_B is Boltzmann's constant and T is temperature. Unfortunately, the acceptance probabilities of these simple switch moves are very low. Since Y^{3+} and Zr^{4+} ions have different ionic radii, the oxygen ions around them are distributed at different distances in equilibrium. Switching the Y^{3+} and Zr^{4+} ions will invariably place these cations in energetically unfavorable positions, and result in a substantial increase in energy.

To enhance acceptance probabilities, we designed a new trial move that also displaces the neighboring ions of the switched cations. The details of this new trial move are as follows.

Let A be the cation that is switched from Y^{3+} to Zr^{4+} and let B be the other one that is switched from Zr^{4+} to Y^{3+} . The new positions of the other ions in the vicinity of A and B are completely specified by two empirical functions, $f(R)$ and $g(R)$, which are inverse functions of each other and are shown in Fig. 2. Notice that $f(R) \leq R$, $g(R) \geq R$, and $f(R) = g(R) = R$ for $R \geq R_c$, where $R_c = 6 \text{ \AA}$ is a cut-off radius. The latter condition implies that any ions that are separated by more than R_c away from the switching cations will not be displaced. The displacements of the ions within the cut-off radius are calculated in two steps.

The first step involves all ions (excluding A and B) whose distances from the cation A are less than R_c . For each ion i , let \mathbf{r}_{Ai} be its displacement vector from cation A and let $R_{Ai} = |\mathbf{r}_{Ai}|$. Ion i is displaced in the \mathbf{r}_{Ai} direction so that its new distance from cation A becomes $r_{Ai} = f(R_{Ai})$. The second step involves all ions (excluding A and B) whose distances from the cation B are less than the cut-off radius. These ions are displaced by the same procedure as in the first step, except that function $g(R)$ is used to calculate the new positions.

Since we always proceed from the neighbors of cation A to those of cation B , it is obvious that two consecutive switch moves involving the same cation pair will restore the positions of all ions, i.e. not only A and B , but also their neighbors. This means that the new MC algorithm satisfies detailed balance, which is essential to sample the proper statistical ensemble.

By trial and error, we found that the following functional form of $f(R)$ gives a reasonable acceptance ratio for this new algorithm:

$$f(R) = \begin{cases} R - \frac{a}{R} + \frac{a}{R_c} & R < R_c \\ R & R \geq R_c \end{cases} \quad (2)$$

where $a = 0.46 \text{ \AA}^2$ for both YSZ and GDC. The new algorithm results in a factor of 5–7 increase in the acceptance ratio of the trial moves.

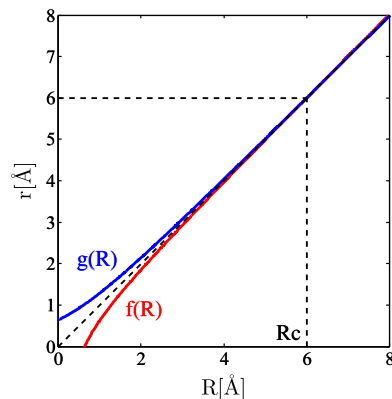


Fig. 2. Empirical functions $f(R)$ and $g(R)$ for displacing the neighboring ions of the switched cation pair.

In the hybrid MC–MD algorithm, an MD simulation is executed every 20 successful MC trial moves. Most of the MD simulations are performed for 20 fs in the NVT ensemble, using the velocity Verlet integrator and Nose–Hoover thermostat [53–55] with a time step of 0.5 fs. One out of every five MD simulations is performed for 100 ps in the NPT ensemble using the Parrinello–Rahman barostat [56]. Overall, the hybrid MC–MD simulation samples the NPT ensemble.

3. Results

Eight YSZ and eight GDC crystals with different initial defect distributions are prepared by the procedure described in Section 2.1. The initial positions of the dopant cations and oxygen vacancies are chosen randomly. Unless otherwise mentioned, the results we present are averaged over the eight systems. Each hybrid MC–MD simulation contains 1×10^7 MC trial steps, which lead to about 3×10^4 – 6×10^4 successful “trial switch moves” at $T = 2000$ K and negligible stress. The simulation results are presented in the following sections.

3.1. Progression toward equilibrium

One way to monitor the progress toward equilibrium is to plot the total energy as a function of the number of successful MC trial moves. Despite considerable fluctuations, a qualitative trend of energy reduction can be observed in Fig. 3 during the first 15,000 successful MC trial moves. Therefore, the equilibrium distributions of ionic species are obtained by averaging over 100 snapshots taken between 15,000 and 30,000 successful MC steps.

3.2. Dopant segregation in YSZ and GDC

Fig. 4a shows the positions of Y^{3+} ions projected onto the x – y plane during the hybrid MC–MD equilibration (superimposing 100 snapshots). Despite their low concentration, Y^{3+} ions seem to have visited almost all cation sites

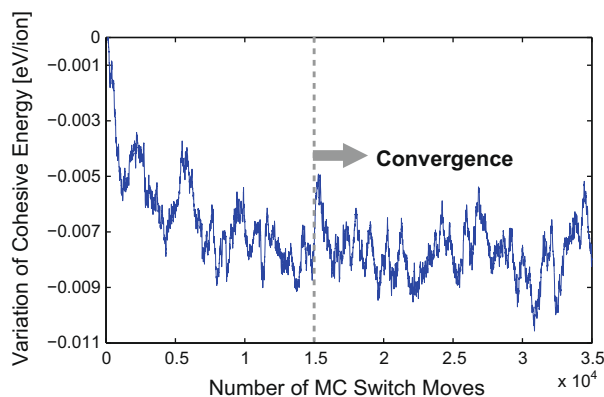


Fig. 3. The variation of the cohesive energy (total energy per ion) of the YSZ crystal as a function of the number of successful MC switch moves at $T = 2000$ K and $p = 0$ MPa.

except for a few in the first cation layers. This suggests that the distribution of Y^{3+} dopants is well equilibrated by the hybrid MC–MD simulations. Fig. 4c and e show the concentration distributions of Y^{3+} and Zr^{4+} ions (in solid lines) along the x -axis, averaged over the snapshots. The concentration profiles at the beginning of the hybrid MC–MD simulations are also presented (in dashed lines) for comparison. In addition, Fig. 4g shows the ratio of the Y^{3+} to Zr^{4+} concentrations as a function of x . On the other hand, Fig. 4b, d, f and h are the corresponding plots for Gd^{3+} and Ce^{4+} ions in GDC.

Fig. 4c clearly shows that Y^{3+} ions segregate to the surfaces in the final structures, in contrast to the noisy profile of the initial structures (dashed line). Interestingly, the equilibrium distribution of the Y^{3+} ions shows the highest concentration peaks in the third cation layers from the surface. In fact, the dopant concentrations in the first cation layers are lower than the average dopant concentration in a bulk crystal. In Fig. 4g, the ratio of Y^{3+} to Zr^{4+} concentrations shows the highest value of 0.35 near the surfaces and stays around 0.24 in the bulk region. The former divided by the mean bulk value of this ratio (0.22 for 10 mol.% YSZ and GDC) gives a surface dopant enrichment factor of 1.6. These values are close to those reported from X-ray photoelectron spectroscopy (XPS), Auger electron spectroscopy (AES) and low-energy ion scattering (LEIS) measurements [1–10], which are summarized in Table 1. We also note that except for the LEIS measurements, the spatial resolutions of these experiments are limited to 20–40 Å and cannot resolve the detailed distribution of dopants in the first few atomic layers. Hence a direct comparison with our simulation data is still problematic. The latest observation from the LEIS experiments shows that the dopant segregation occurs on the length scale of a few atomic layers [8], which agrees well with our simulation results.

Fig. 4d shows the concentration profile of Gd^{3+} ions in GDC, which also exhibits near-surface dopant segregation. Unlike the distribution of Y^{3+} ions in YSZ, however, the highest concentration of Gd^{3+} ions appears in the first cation layers. Interestingly, there are also signs of dopant depletion beginning at the fourth cation layers. In Fig. 4h, the ratio of Gd^{3+} to Ce^{4+} concentrations shows the highest value of 0.68 in the first cation layers and about 0.18 in the center. The enrichment factor of Gd^{3+} in the first cation layers with respect to the mean bulk value is estimated to be about 3.1. These predictions are in good agreement with LEIS experiments, where the surface Gd^{3+} to Ce^{4+} ratio and the enrichment factor are about 1.00 and 4.2, respectively [11]. The LEIS measurements also show that the dopant segregation occurs intensively within five atomic layers from the surface, which agrees well with our simulation results.

3.3. Oxygen vacancy distributions in YSZ and GDC

The hybrid MC–MD simulations also allow us to examine the equilibrium distributions of oxygen vacancies,

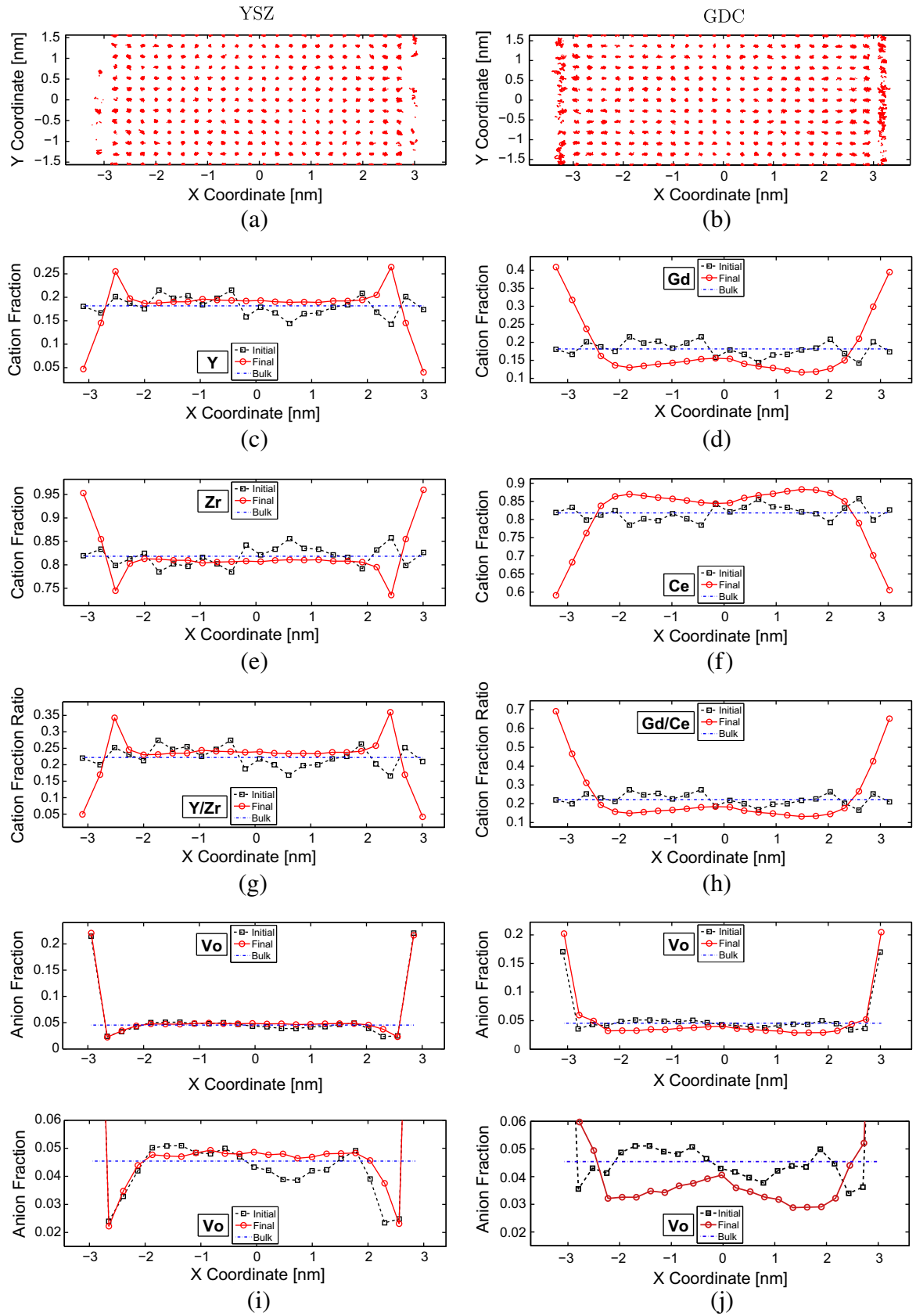


Fig. 4. Dopant cation positions projected onto the x - y plane for (a) YSZ and (b) GDC. Dopant cation fraction distribution along x -axis for (c) YSZ and (d) GDC. Host cation fraction distribution for (e) YSZ and (f) GDC. The ratio of dopant and host cation fractions for (g) YSZ and (h) GDC. Vacancy anion fraction in (i) YSZ and (j) GDC ($T = 2000$ K and $p = 0$ MPa).

Table 1
X-ray photoelectron spectroscopy (XPS), Auger electron spectroscopy (AES) and low-energy ion scattering (LEIS) measurements on surface segregation of dopants in YSZ.

| References | Method(s) | Y ₂ O ₃ content (mol.%) | Temperature (K) | Surface Y/Zr ratio | Enrichment factor |
|-------------------------|-----------|-----------------------------------------------|-----------------|--------------------|-------------------|
| Theunissen et al. [1,7] | AES | 7.0 | 1273 | 0.52 | 2.95 |
| | | 9.3 | 1273 | 0.45 | 1.98 |
| Hughes and Sexton [2] | XPS | 10.0 | 1573 | 0.34 | 1.45 |
| | | 10.0 | 1623 | 0.34 | 1.45 |
| | | 10.0 | 1673 | 0.34 | 1.45 |
| | | 10.0 | 1723 | 0.32 | 1.38 |
| | | 10.0 | 1773 | 0.37 | 1.56 |
| | | 10.0 | 1873 | 0.36 | 1.53 |
| | | 10.0 | 1973 | 0.36 | 1.53 |
| Hughes [4] | XPS | 9.5 | 1373 | 0.30 | 1.37 |
| | | 9.5 | 1373 | 0.32 | 1.45 |
| | | 9.5 | 1573 | 0.30 | 1.37 |
| | | 9.5 | 1573 | 0.35 | 1.57 |
| de Ridder et al. [8] | LEIS | 10.0 | 1423 | 0.44 | 3.00 |
| Bernasik et al. [9] | XPS | 8.0 | 1273 | 0.18 | 1.24 |
| | | 8.0 | 1473 | 0.22 | 1.62 |
| | | 8.0 | 1673 | 0.30 | 1.35 |

which are shown in Fig. 4i and j for YSZ and GDC, respectively. Since the cation sublattice remains mostly crystalline and relatively stable during the MC–MD simulations, it can be used as a reference structure to determine the local oxygen vacancy concentration. The number of oxygen vacancies in any anion layer can be calculated by subtracting the number of oxygen ions between the two neighboring cation layers from the total number of anion sites based on the cubic (CaF₂) structure of the perfect crystal. The leftmost and rightmost points in Fig. 4i and j correspond to the anion layers between the first and second cation layers from the surface. For convenience, we define them as the first anion layers in the following discussion. The actual surface layers (outmost), as briefly mentioned in the initialization step, consist of a number of oxygen ions and are not included in Fig. 4i and j.

The equilibrium oxygen vacancy distributions (solid lines) show the highest concentrations in the first anion layers of both YSZ and GDC. The high concentration of oxygen vacancies on the (001) surface of YSZ qualitatively agrees with the MEIS measurements [57]. In contrast, the oxygen vacancy concentration in the next two anion layers (second and third) of YSZ drops below the mean bulk value, resulting in a near-surface depletion. In GDC, it is still slightly above the mean bulk value in the second and third anion layers, but again falls below the mean bulk value after the fourth layers (and almost over the entire system). Since space-charge theory [15–20] predicts the depletion of oxygen vacancies in the space-charge layers, it is tempting to interpret the simulation results as a confirmation of space-charge theory. However, the atomistic simulations also reveal many details that contradict the predictions based on space-charge theory. For example, space-charge theory predicts a negative correlation between the distributions of dopant cations and oxygen vacancies,

in which the dopant segregation and oxygen vacancy depletion occur in the same region. While one may think that this is observed in our simulations of YSZ in Fig. 4g and i, it is not compatible with our simulation results of GDC in Fig. 4h and j, where dopant and oxygen vacancy concentration distributions are positively correlated with each other.

4. Discussions

In this section, we examine simulation results in further detail and investigate the effects of defect association on the equilibrium distributions of the point defects. First, we notice from Fig. 4i and j that there are high concentrations of oxygen vacancies in the first anion layers even in the initial structures with randomly distributed dopants (after the initial MD relaxation). Therefore, the high near-surface content of the oxygen vacancies is not a consequence of dopant segregation; rather, the reverse is likely to be true. When the dopant cations are allowed to move in the hybrid MC–MD simulations, they are likely to segregate toward the surface due to the dopant cation–oxygen vacancy association. Since Y³⁺ ions are less likely to have oxygen vacancies as their first nearest-neighbors than Gd³⁺ ions [25,29,35,36,38,40,41,43–50], the equilibrium distributions of Y³⁺ and Gd³⁺ ions differ significantly near the surfaces, as shown in Fig. 4c and d.

4.1. Vacancy distribution before and after dopant segregation

In Fig. 4i and j, the high concentration of oxygen vacancies in the first anion layers can be attributed to the low formation energy within close proximity of surfaces, which is in good agreement with MEIS measurements and ab initio

calculations [57–59]. On the other hand, depletion in the inner layers is due to the Coulomb repulsion between oxygen vacancies. If we assume space-charge theory accounts for this behavior, then the vacancy depletion layers can be interpreted as space-charge layers with a thickness of about 10–15 Å in both YSZ and GDC.

Interestingly, after the dopant cations are allowed to move to different sites, the oxygen vacancies are redistributed in distinctly different ways in YSZ and GDC. In YSZ, the aggregation of oxygen vacancies in the first anion layer and depletion in adjacent layers are reduced, whereas in GDC both aggregation and depletion become more pronounced. In other words, the near-surface segregation of Y^{3+} ions in YSZ counteracts the driving force for segregation of oxygen vacancies, while the opposite is true in GDC. The redistribution of cations also causes greater changes in the oxygen vacancy distribution in GDC than that in YSZ. After the segregation in a few layers close to the surface, both Gd^{3+} and $V_{O^{2-}}$ are depleted over a wide range further away from the surface. However, the depletion of Gd^{3+} and $V_{O^{2-}}$ in this range cannot be interpreted as a space-charge effect, because these two species are being depleted at the same time, exhibiting a positive correlation.

4.2. Dopant–vacancy association

Space-charge theory predicts a negative correlation between the near-surface equilibrium distributions of dop-

ant cations and oxygen vacancies. On the other hand, since dopant cations and oxygen vacancies have opposite effective charges, the Coulomb attraction is likely to cause a positive correlation between them. To test these hypotheses, we plot oxygen vacancy concentrations against dopant concentrations in both YSZ and GDC, which are shown in Fig. 5a and b, respectively. Since cation and anion layers alternate in the crystal, the x -coordinate of each data point is the averaged value of the dopant concentrations of the two cation layers neighboring the anion layer (this layer corresponds to the y -coordinate). While no distinct trend can be observed in YSZ, a positive correlation is clearly seen in GDC, contradicting the prediction of the space-charge theory.

In Fig. 5c and d, we examine the correlation between the concentration variations (before and after dopant segregation) of the dopant cations and oxygen vacancies in YSZ and GDC. In Fig. 5c, a weak positive correlation can be observed in the bulk region of YSZ, but it becomes indistinct near the surface. In comparison, Fig. 5d shows a pronounced positive correlation in both bulk and near-surface regions of GDC (first, second and third layers).

To gain a better understanding of the dopant–oxygen vacancy association effects, we investigate the average coordination numbers of oxygen ions around dopant and host cations in bulk YSZ and GDC crystals, which are free from interfacial effects. Each crystal is 6 nm × 6 nm × 6 nm in size with dopant cations and oxygen vacancies randomly distributed. Eight systems with different (random)

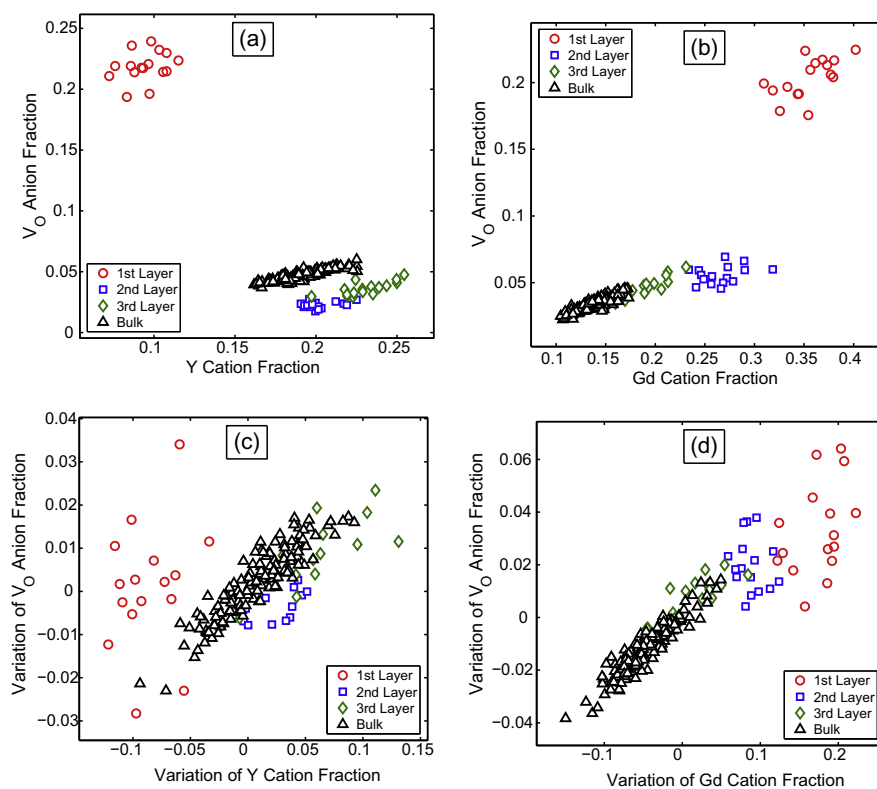


Fig. 5. Correlations between the equilibrium dopant cation and oxygen vacancy concentrations in (a) YSZ and (b) GDC. Correlations between the concentration variations of dopant cations and oxygen vacancies caused by surface segregation in (c) YSZ and (d) GDC. Doping concentration is set to 10 mol. % for both materials the simulations are carried out at $T = 2000$ K and $p = 0$ MPa.

initial defect distributions are created for each material and the results are averaged out. MD simulations are carried out for 200 ps with a time step of 0.5 fs at $T = 2000$ K and $p = 0$ MPa in an NPT ensemble to equilibrate the structures. After the MD simulations, the average numbers of first and second nearest-neighbor oxygen (NNO) ions around Y^{3+} , Zr^{4+} , Gd^{3+} and Ce^{4+} ions are calculated and these are presented in Table 2.

At equilibrium, Y^{3+} ions have more first-NNOs and fewer second-NNOs than Zr^{4+} ions. This suggests that oxygen vacancies prefer to be the second nearest-neighbors of Y^{3+} ions but not their first nearest-neighbors. On the other hand, Gd^{3+} ions have fewer first-NNOs and fewer second-NNOs than Ce^{4+} ions, implying that both first and second nearest-neighbor positions around Gd^{3+} cations are energetically favorable for the oxygen vacancies. These findings are consistent with the correlation plots in Fig. 5 as well as previous studies [25,29,35,36,38,40,41,43–50]. However, the tendency of oxygen vacancies to associate with cations does not lead to well-defined defect complexes, probably because of the high temperatures in the simulations.

4.3. Driving force for defect segregation

Even though several mechanisms have been proposed in a number of studies to explain the driving forces of dopant segregation at the surfaces of YSZ and GDC, fundamental questions still remain unanswered as to which one of those factors is the most dominant. An example of the driving forces is the elastic strain caused by the size mismatch between dopant and host cations. Since a Y^{3+} or Gd^{3+} ion has a larger ionic radius than a Zr^{4+} or Ce^{4+} ion, the elastic strain energy of the system due to this size mismatch can be reduced if Y^{3+} or Gd^{3+} ions segregate to the surfaces, where more free volume is available. However, if this was the dominant factor, then it would be unclear why the dopant segregation is more pronounced in GDC than YSZ

when the ionic size mismatch between Y^{3+} and Zr^{4+} is 87.5% greater than that between Gd^{3+} and Ce^{4+} .

On the other hand, space-charge theory predicts that the interfacial segregation can occur even without any ionic size mismatch or elastic effects. Instead, the difference between the formation energies of cation and anion vacancies gives rise to different interfacial concentrations of these defects and therefore an electric potential field, which affects the equilibrium distributions of charged species near the interfaces. Since dopant cations and oxygen vacancies have opposite effective charges in YSZ and GDC, they respond to the mean-field Coulomb potential in opposite ways. As a result, dopant segregation will occur in the vicinity of the surfaces and will accompany near-surface depletion of the oxygen vacancies. The negative correlation between dopants and oxygen vacancies, however, is contrary to our simulation results of GDC, which clearly shows a positive correlation.

Our atomistic simulations suggest a different mechanism for dopant segregation than those mentioned above. According to Fig. 4i and j, oxygen vacancies segregate to the first anion layers in the initial structures even without dopant segregation. As the hybrid MC–MD simulation enables the redistribution of the cations, dopants will rearrange themselves in response to the long-range and short-range interactions with oxygen vacancies. As seen in Section 4.2, the correlation between dopant cations and oxygen vacancies is different between YSZ and GDC, and explains the difference in the dopant segregation profile. In YSZ, Y^{3+} ions prefer the oxygen vacancies as the second nearest-neighbors but not as the first nearest-neighbors. Since the oxygen vacancies are aggregated in the first anion layers but depleted in the second and third anion layers, Y^{3+} ions are likely to avoid the first cation layers and prefer the third layer. This effect is stronger than the elastic strain effect caused by the mismatch of ionic radii, because the first two cation layers show depletion of dopants, despite the elastic driving force for the dopant segregation. In GDC, on the other hand, Gd^{3+} ions prefer the oxygen vacancies as both first and second nearest-neighbors. As a result, the concentration of Gd^{3+} ions in the first three cation layers is above the mean bulk value. While the long-range Coulomb interaction (which is accounted for in space-charge theory) must have played a role here, the positive correlation between Gd^{3+} and $V_{O^{2-}}$ concentrations is opposite to the predictions of space-charge theory.

Table 2
Mean first- and second-nearest-neighbor oxygen (NNO) coordination numbers for YSZ and GDC.

| Species | First-NNO coordination | Second-NNO coordination |
|-----------|------------------------|-------------------------|
| Zr^{4+} | 7.37 | 31.09 |
| Y^{3+} | 7.83 | 30.09 |
| Ce^{4+} | 7.72 | 29.95 |
| Gd^{3+} | 7.60 | 29.50 |

Table 3
BMB potential parameters for YSZ and GDC.

| Interaction | A_{ij} (eV Å ⁶) | B_{ij} (eV) | C_{ij} (Å) | References |
|------------------|-------------------------------|---------------|--------------|--------------------------|
| $Y^{3+}-O^{2-}$ | 0.0 | 1345.1 | 0.3491 | Lewis and Catlow [51] |
| $Zr^{4+}-O^{2-}$ | 0.0 | 985.869 | 0.376 | Dwivedi and Cormack [52] |
| $O^{2-}-O^{2-}$ | 27.890 | 22764.300 | 0.149 | Dwivedi and Cormack [52] |
| $Gd^{3+}-O^{2-}$ | 20.34 | 1885.75 | 0.3399 | Minervini et al. [39] |
| $Ce^{4+}-O^{2-}$ | 20.40 | 1809.68 | 0.3547 | Minervini et al. [39] |
| $O^{2-}-O^{2-}$ | 32.0 | 9547.96 | 0.2192 | Minervini et al. [39] |

The above mechanism explains why Y^{3+} segregation in YSZ is less pronounced than Gd^{3+} segregation in GDC. In spite of the elastic driving force, the high concentration of oxygen vacancies in the first anion layers prevents the local enrichment of the Y^{3+} dopants in the close vicinity of the surfaces. In other words, the greater elastic driving force in YSZ (than in GDC) is partially countered by the dopant–oxygen vacancy interaction. On the other hand, dopant–oxygen vacancy association in GDC works together with the elastic driving force and promotes surface segregation of both dopants and oxygen vacancies.

5. Summary

We developed a hybrid MC–MD algorithm to study the equilibrium distributions of defects in YSZ and GDC thin films. Both dopant cations and oxygen vacancies are observed to segregate near the surface. The concentration of Y^{3+} ions is highest at the third cation layer from the surface in YSZ, whereas the concentration of Gd^{3+} ions is highest at the first cation layer in GDC. The differences in the equilibrium distributions of the point defects between YSZ and GDC are likely to affect the ionic transport and chemical reactions in different ways near the surface. Our simulation results suggest that the interaction between point defects, which is neglected in the existing applications of space-charge theory to YSZ, plays a major role in the interfacial dopant segregation of the ionic oxides. This effect is stronger than the elastic strain caused by the ionic size mismatch between dopant and host cations and makes the dopant segregation more pronounced in GDC despite the greater ionic size mismatch in YSZ.

Acknowledgements

This work is supported by a DOE/SciDAC Project on Quantum Simulation of Materials and Nanostructures and an NSF/CMMI Nano Bio Materials Project CMS-0556032.

Appendix. Interatomic potentials

The potential energy as a function of the ionic positions, \mathbf{r}_i ($i = 1, \dots, N$) can be written as:

$$\begin{aligned}
 V(\{\mathbf{r}_i\}) &= V_{\text{MBM}}(\{\mathbf{r}_i\}) + V_{\text{Coulomb}}(\{\mathbf{r}_i\}) \\
 &= \sum_{i=1}^{N-1} \sum_{j=i+1}^N \left[-\frac{A_{ij}}{|r_{ij}|^6} + B_{ij} \exp(-C_{ij}|r_{ij}|) \right] \\
 &\quad + \sum_{i=1}^{N-1} \sum_{j=i+1}^N \frac{q_i q_j}{|r_{ij}|} \quad (3)
 \end{aligned}$$

where q_i is the effective charge of ion i and equals $+4e$, $+3e$ and $-2e$ for Zr^{4+}/Ce^{4+} , Y^{3+}/Gd^{3+} and O^{2-} ions, respectively. $r_{ij} = |\mathbf{r}_j - \mathbf{r}_i|$ is the distance between ion i and j . The short-range potential parameters A_{ij} , B_{ij} and C_{ij} are taken from the literature [51,52,39] and depend on the species

of ions i and j (see Table 3). The long-range Coulomb potential is computed by either classical Ewald [61] or particle mesh Ewald [62,63] methods in different parts of the simulation. All calculations are performed by MD++ [64].

References

- [1] Theunissen GSAM, Winnubst AJA, Burggraaf AJ. J Mater Sci Lett 1989;8:55.
- [2] Hughes AE, Sexton BA. J Mater Sci 1989;24:1057.
- [3] Hughes AE, Badwal SPS. Solid State Ionics 1990;40/41:312.
- [4] Hughes AE. PhD thesis, Royal Melbourne Institute of Technology; 1991.
- [5] Hughes AE, Badwal SPS. Solid State Ionics 1991;46:265.
- [6] Majumdar D, Chatterjee D. J Appl Phys 1991;70(2):988.
- [7] Theunissen GSAM, Winnubst AJA, Burggraaf AJ. J Mater Sci 1992;27:5057.
- [8] de Ridder M, van Welzenis RG, Denier van der Gon AW, Brongersma HH, Wulff S, Chu W-F, et al. J Appl Phys 2002;92(6):3056.
- [9] Bernasik A, Kowalski K, Sadowski A. J Phys Chem Solids 2002;63:233.
- [10] Nowotny J, Sorrell CC, Bak T. Surf Interface Anal 2005;37:316.
- [11] Scanlon PJ, Bink RAM, van Berkel FPF, Christie GM, van IJzendoorn LJ, Brongersma HH, et al. Solid State Ionics 1998;112:123.
- [12] Kokai F, Amano K, Ota H, Ochiai Y, Umemura F. J Appl Phys 1992;72:699.
- [13] Chour K-W, Chen J, Xu R. Thin Solid Films 1997;304:106.
- [14] Putkonen M, Sajavaara T, Niinisto J, Johansson LS, Niinisto L. J Mater Chem 2002;12:442.
- [15] Guo X. Solid State Ionics 1995;81:235.
- [16] Guo X, Maier J. J Electrochem Soc 2001;148:E121.
- [17] Guo X, Sigle W, Fleig J, Maier J. Solid State Ionics 2002;154–155:555.
- [18] Guo X, Zhang Z. Acta Mater 2003;51:2539.
- [19] Guo X, Waser R. Solid State Ionics 2004;173:63.
- [20] Guo X, Ding Y. J Electrochem Soc 2004;151(1):J1.
- [21] Kliewer KL, Koehler JS. Phys Rev A 1965;140(4A):A1226.
- [22] Kliewer KL. Phys Rev A 1965;140(4A):A1241.
- [23] Yan MF, Cannon RM, Bowen HK. J Appl Phys 1983;54:764.
- [24] Chiang YM, Birnie III DP, Kingery WD, editors. Physical ceramics: principles for ceramic science and engineering. New York: John Wiley; 1997. p. 155.
- [25] Shimojo F, Okabe T, Tachibana F, Kobayashi M, Okazaki H. J Phys Soc Jpn 1992;61(8):2848.
- [26] Shimojo F, Okazaki H. J Phys Soc Jpn 1992;61(11):4106.
- [27] Okazaki H, Suzuki H, Ihata K. Phys Lett A 1994;188:291.
- [28] Okazaki H, Suzuki H, Ihata K. J Phys Soc Jpn 1994;63(1):3556.
- [29] Li X, Hafskjold B. J Phys Condens Matter 1995;7:1255.
- [30] Brinkman HW, Briels WJ, Verweij H. Chem Phys Lett 1995;247:386.
- [31] Fisher CAJ, Matsubara H. Solid State Ionics 1998;113:311.
- [32] Khan MS, Islam MS, Bates DR. J Mater Chem 1998;8:2299.
- [33] Fisher CAJ, Matsubara H. J Eur Ceram Soc 1999;19:703.
- [34] Fisher CAJ, Matsubara H. Comput Mater Sci 1999;14:177.
- [35] Yamamura Y, Kawasaki S, Sakai H. Solid State Ionics 1999;126:181.
- [36] Zacate MO, Minervini L, Bradfield DJ, Grimes RW, Sickafus KE. Solid State Ionics 2000;128:243.
- [37] Tang YW, Zhang Q, Chan K. Chem Phys Lett 2004;385:202.
- [38] Devanathan R, Thevuthasan S, Gale JD. Phys Chem Chem Phys 2009;11:5506.
- [39] Minervini L, Zacate MO, Grimes RW. Solid State Ionics 1999;116:339.
- [40] Inaba H, Sagawa R, Hayashi H, Kawamura K. Solid State Ionics 1999;122:95.
- [41] Hayashi H, Sagawa R, Inaba H, Kawamura K. Solid State Ionics 2000;131:281.

- [42] Hayashi H, Kanoh M, Quan CJ, Inaba H, Wang S, Dokiya M, et al. *Solid State Ionics* 2000;132:227.
- [43] Catlow CRA, Chadwick AV, Greaves GN, Moroney RM. *J Am Ceram Soc* 1986;69:272.
- [44] Veal BW, McKale AG, Paulikas AP, Rothman SJ, Nowicki LJ. *Physica B* 1988;150:234.
- [45] Komyoji D, Yoshiasa A, Moriga T, Emura S, Kanamaru F, Koto K. *Solid State Ionics* 1992;50:291.
- [46] Li P, Chen I-W, Penner-Hahn JE. *Phys Rev B* 1993;48(14):10074.
- [47] Goff JP, Hayes W, Hull S, Hutchings MT, Clausen KN. *Phys Rev B* 1999;59(22):14202.
- [48] Stapper G, Bernasconi M, Nicoloso N, Parrinello M. *Phys Rev B* 1999;59:797.
- [49] Kawata K, Maekawa H, Nemoto T, Yamamura T. *Solid State Ionics* 2006;177:1687.
- [50] Pietrucci F, Bernasconi M, Laio A, Parrinello M. *Phys Rev B* 2008;78:094301.
- [51] Lewis GV, Catlow CRA. *J Phys C Solid State Phys* 1985;18:1149.
- [52] Dwivedi A, Cormack AN. *Philos Mag A* 1990;61(1):1.
- [53] Nose S. *Mol Phys* 1984;52(2):255.
- [54] Nose S. *J Chem Phys* 1984;81(1):511.
- [55] Hoover WG. *Phys Rev A* 1985;31(3):1695.
- [56] Parrinello M, Rahman A. *J Appl Phys* 1981;52:7182.
- [57] Nishimura T, Toi H, Hoshino Y, Toyoda E, Kido Y. *Phys Rev B* 2001;64:073404.
- [58] Eichler A, Kresse G. *Phys Rev B* 2004;69:045402.
- [59] Ballabio G, Bernasconi M, Pietrucci F, Serra S. *Phys Rev B* 2004;70:075417.
- [60] Metropolis N, Rosenbluth AW, Rosenbluth MN, Teller AH, Teller E. *J Chem Phys* 1953;21(6):1087.
- [61] DeLeeuw SW, Perram JW, Smith ER. *Proc Roy Soc London Ser A* 1980;373:27.
- [62] Darden T, York DM, Pedersen LG. *J Chem Phys* 1993;98(12):10089.
- [63] Essmann U, Perera L, Berkowitz ML, Darden T, Lee H, Pedersen LG. *J Chem Phys* 1995;103(19):8577.
- [64] MD++ code. <<http://micro.stanford.edu>>.